An integrated experimental-numerical study of martensite/ferrite interface damage initiation in dual-phase steels

Liu, L.; Maresca, F.; Vermeij, T.; Hoefnagels, J. P.M.; Geers, M. G.D.; Kouznetsova, V. G.

Published in:
Scripta Materialia

DOI:
10.1016/j.scriptamat.2023.115798

Scripta Materialia 239 (2024) 115798

Contents lists available at ScienceDirect

Scripta Materialia

journal homepage: www.journals.elsevier.com/scripta-materialia

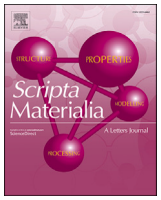

An integrated experimental-numerical study of martensite/ferrite interface damage initiation in dual-phase steels

L. Liu [a,b], F. Maresca [c], T. Vermeij [a,b], J.P.M. Hoefnagels [a], M.G.D. Geers [a], V.G. Kouznetsova [a,*]

[a] Department of Mechanical Engineering, Eindhoven University of Technology, 5600 MB Eindhoven, The Netherlands
[b] Materials Innovation Institute (M2i), 2600 GA Delft, The Netherlands
[c] Engineering and Technology Institute Groningen, Faculty of Science and Engineering, University of Groningen, 9747 AG Groningen, The Netherlands

ARTICLE INFO

Keywords:
Dual-phase steel
Martensite/ferrite interface
Damage initiation
Substructure boundary sliding
Experimental-numerical study

ABSTRACT

Martensite/ferrite (M/F) interface damage is relevant to failure of many dual-phase (DP) steels, but the underlying microscale mechanisms remain unclear. Through an integrated experimental-numerical study, this work examines the recent hypothesis that (lath) martensite substructure boundary sliding triggers and dominates M/F interface damage initiation accompanied by apparent martensite plasticity. The mesoscale morphology and prior austenite grain reconstruction are used as modelling inputs. A multi-scale framework is adopted to predict the interface damage initiation. The M/F interface damage initiation sites predicted by the model based on a sliding-triggered interface damage mechanism adequately agree with those identified from in-situ experiments, confirming the key role of substructure boundary sliding. Moreover, the M/F interface damage initiation strongly correlates with a low M/F strain partitioning rather than the commonly accepted strong M/F strain partitioning. This fundamental understanding is instrumental for the future optimization of DP steel microstructures.

Despite a variety of attempts to optimize the mechanical properties, the full potential of DP steels remains limited by the well-known strength/ductility trade-off [1]. In particular, the underlying microscale mechanisms that cause failure and hence control ductility, are not yet fully understood. Extensive experimental observations have shown that M/F interface damage is relevant to failure of many DP steels, especially those with low (10%) to moderate (50%) martensite volume fractions (e.g. [2–4]). Commonly, M/F interface damage is expected to originate from the large M/F phase contrast since martensite is regarded as a hard constituent compared to ferrite (e.g. [5–8]). This understanding, however, is contradicted by recent experimental observations (e.g. DP600 [9], DP800 [10,11] and DP1000 [12]), showing interface damage accompanied by apparent martensite plasticity.

Lath martensite has a complex hierarchical structure with many internal boundaries [13–15], which can induce misfit among different oriented laths and trigger martensite cracking [16,10,17–19]. Nevertheless, for a single martensite island (or band) in DP steels, the substructure boundaries are almost parallel to the same habit plane (e.g. [20,21]). Moreover, nanoscale inter-lath retained austenite (RA) films can exist at these boundaries (e.g. martensitic steels [22–24] and DP steels [25,26]). Crystal plasticity and atomistic simulations [27–30] have shown that these RA films can trigger pronounced substructure boundary sliding, originating from the crystallographic slip (promoted by the specific martensite/austenite (M/A) crystallographic orientation relationship (OR) and the lower slip resistance of the FCC RA films compared to the BCC laths) and/or the phase transformation. Extensive experimental evidence for this sliding mechanism has also been reported (e.g. martensitic steels [31–33] and DP steels [34–38]), showing that the substructure boundaries can undergo extremely large sliding without fracture.

Recent crystal plasticity simulations [39] indicated that the substructure boundary sliding might also trigger and dominate M/F interface damage initiation upon the occurrence of apparent martensite plasticity. This sliding-triggered interface damage mechanism has been supported by experimental observations [40]. In this work, an integrated experimental-numerical study is conducted to examine this hypothesis [39] and gain further insights for the interface damage initiation. The interface damage initiation is predicted numerically by applying the recently developed multi-scale framework [41] on the experimental mesoscale morphology and crystallography. The predicted damage initiation sites are compared against those observed in the experiments.

* Corresponding author.
E-mail address: v.g.kouznetsova@tue.nl (V.G. Kouznetsova).

https://doi.org/10.1016/j.scriptamat.2023.115798
Received 4 July 2023; Received in revised form 26 August 2023; Accepted 27 September 2023
Available online 13 October 2023

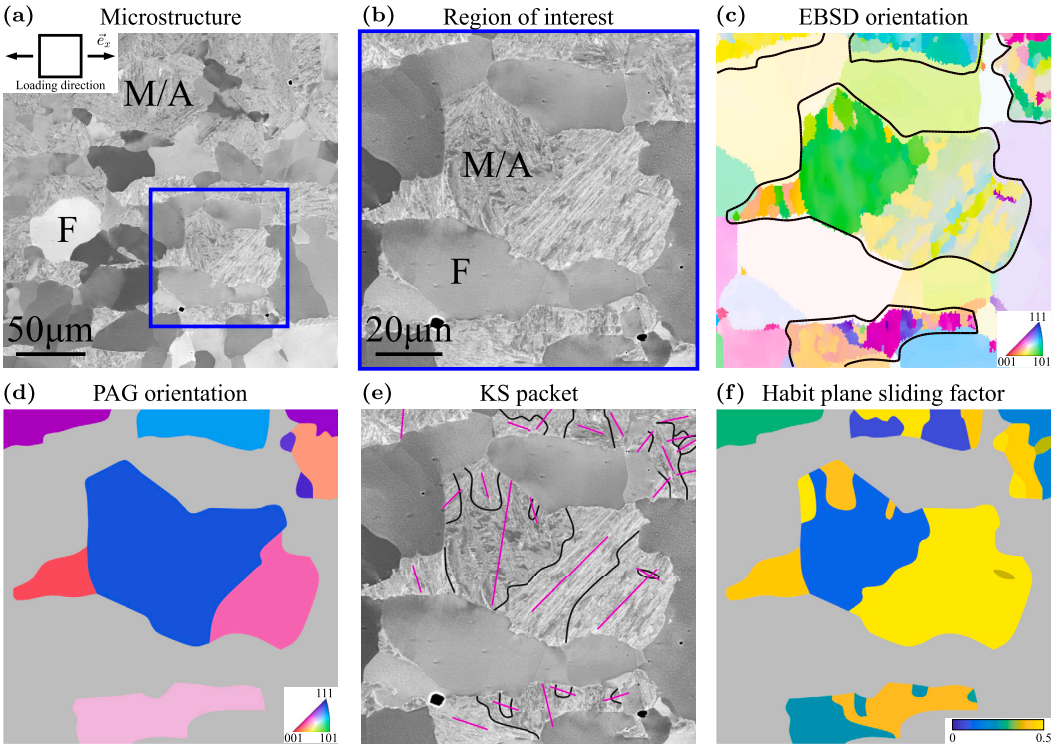

Fig. 1. (a) SEM micrograph of the DP steel microstructure area before deformation, showing several martensite islands (martensite/austenite laminates, M/A) embedded in a ferrite matrix; (b) magnification of the region of interest (blue box); (c) EBSD crystallographic orientation map of the martensite and ferrite grains. Black lines indicate the M/F interfaces, as determined from (b); (d) the PAG crystallographic orientation map; (e) the Kurdjumov-Sachs (KS) packets separated by the black lines. The in-plane projections of the habit plane traces within individual packets are indicated by the pink lines; (f) the so-called habit plane sliding factor map, computed with respect to the horizontal loading direction $\vec{e}_x$. (For interpretation of the colours in the figure(s), the reader is referred to the web version of this article.)

Experimental specimens were prepared from a heat-treated DP600 (Fe-0.092C-1.68Mn-0.57Cr-0.24Si wt.%). The as-received steel sheet was first annealed for 10 minutes at 1100 °C and then intercritically annealed for 30 minutes at 750 °C, followed by water quenching to room temperature. The resulting DP steel microstructure revealed a martensite volume fraction ~ 60% and martensite island sizes 50–100 μm. After the heat treatment, specimens with dimensions 30 mm × 10 mm × 1 mm were cut, followed by mechanical grinding and polishing with colloidal silica for 30 minutes.

Hemming tests were carried out on the prepared specimens. A microstructure area, Fig. 1(a), with an overall stress state close to uniaxial tension [42], was tracked. One region containing a large martensite island with a clearly visible substructure, Fig. 1(b), is focused. The crystallographic orientations of the individual grains, Fig. 1(c), were mapped with Electron BackScatter Diffraction (EBSD) employing spherical indexing [43]. A misorientation threshold of 2.5° was chosen to identify individual martensite sub-blocks. Based on the martensite crystallography data and considering the Kurdjumov-Sachs (KS) orientation relationship, prior austenite grains (PAG) as well as martensite packets and (sub-)blocks were reconstructed using the PAG reconstruction toolbox in MTEX [44], see [38,45] for more details. The resulting PAG crystallographic orientation map and KS packets (or variant groups, according to the variant list in [14]), together with the in-plane projections of the habit plane trace, are shown in Figs. 1(d) and (e), respectively. As expected, the clearly visible lath boundaries are approximately parallel to the corresponding habit plane traces. A habit plane sliding factor is defined as $f^{\mathrm{hp}} = \cos\phi^{\mathrm{hp}} \sin\phi^{\mathrm{hp}}$, with $\phi^{\mathrm{hp}} = \arccos(\vec{N}^{\mathrm{hp}} \cdot \vec{e}_x)$, the angle between the habit plane normal $\vec{N}^{\mathrm{hp}}$ and the local loading direction $\vec{e}_x$, indicating how favourable the sliding is within each packet (see also [37,38]). The resulting habit plane sliding factor map is shown in Fig. 1(f).

Numerical simulation of the region of interest (Fig. 1(b)) was conducted using a multi-scale framework [41]. Two scales are considered: *mesoscale* representing the DP steel structure consisting martensite islands in a ferrite matrix, and *microscale* resolving the martensite substructure consisting of laths and RA films. The mesostructure is assumed to be invariable in the out-of-plane direction (Z axis). The in-plane mesostructure model is constructed from Fig. 1(b) and shown in Fig. 2(a). To mitigate potential artificial boundary effects [46], a ferrite buffer layer with a width of 5 μm has been added accordingly. It has been verified that the simulation results are insensitive to the choice of the buffer layer width. Within each martensite packet, a RA volume fraction of 10%[1] is assumed (see also [41]), i.e. ~ 5% over the whole DP steel. The crystallographic orientations of the BCC laths and RA films are assigned according to Figs. 1(c) and (d), respectively. For the ferrite matrix, the crystallographic orientation effects are neglected, and an isotropic elasto-(visco-)plasticity model is used [41]. For the martensite islands, a reduced lath martensite model (Fig. 2(b)) is adopted. The martensite packet is described by a lamella model, which represents a stack of laths and RA films [28]. The FCC RA films are described by a reduced crystal plasticity model [47], where only the three slip systems parallel to the habit plane are incorporated, while the plastic deformation in other directions is modelled by von Mises (visco-)plasticity. The relatively hard martensite laths are represented using isotropic elasto-(visco-)plasticity. For the damage initiation prediction at the M/F interfaces (with normal $\vec{N}_{\mathrm{M/F}}$), a microphysics-based interface damage indicator model (Fig. 2(c)) [41] is employed. This model relies on the

[1] It has been shown in [27] that the martensite substructure boundary sliding mechanism and its overall orientation-dependent response are only weakly affected by varying the RA volume fraction as long as this value is chosen to be sufficiently small (≤ 10%).

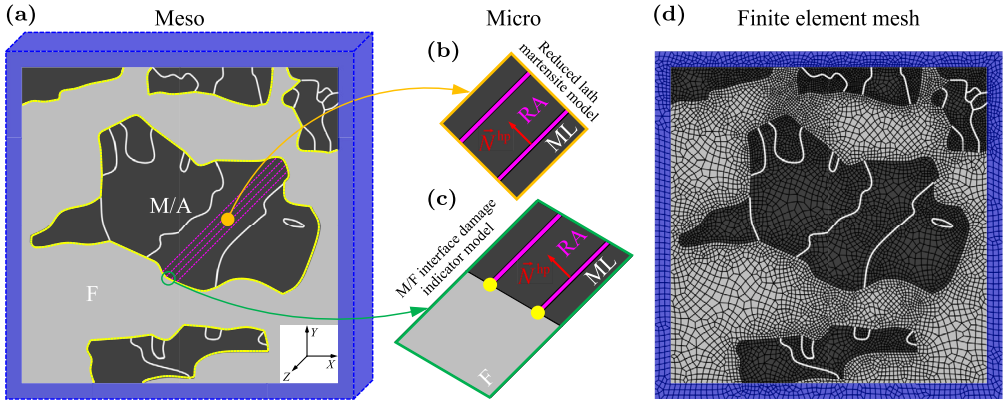

Fig. 2. (a-c) The multi-scale framework adopted to predict the M/F interface damage initiation sites in the DP steel region of interest shown in Fig. 1(b). The mesoscopic M/F interfaces and KS packet boundaries are indicated by the yellow and white lines, respectively. The ferrite buffer layer around the DP steel mesoscale model is indicated by the blue shadow. The underlying martensite substructure which consists of a stack of martensite laths (ML) and RA films, is not spatially resolved at the mesoscale, but accounted for through the microphysics-based constitutive relations: (b) the reduced lath martensite model for the interior of martensite island and (c) the interface damage indicator model for the M/F interfacial zone. The sliding-triggered damage hot spot locations in the M/F interface microstructure are indicated by the yellow dots; (d) the adopted in-plane finite element discretization.

Table 1
Isotropic plasticity model parameters of the ferrite matrix and martensite lath. The model parameters of the RA film are the same as used in [41] and thus not listed here.

Parameter	Ferrite matrix	Martensite lath
Reference strain rate	0.01 [s^{-1}]	0.01 [s^{-1}]
Initial yield stress	0.450 [GPa]	1.504 [GPa]
Saturation yield stress	1.065 [GPa]	5.900 [GPa]
Reference hardening modulus	9.301 [GPa]	16.51 [GPa]
Strain rate sensitivity	0.05 [-]	0.05 [-]
Hardening exponent	0.8 [-]	1.5 [-]

hypothesis [39], that the substructure boundary sliding dominates the interface damage initiation by inducing large plastic strain concentrations in the near-interface ferrite around the RA film tips, acting as damage 'hot spot' locations (yellow dots in Fig. 2(c)). The effective interface damage indicator is a function of the effective sliding representing the overall martensite shear deformation along the habit plane, and depends on the relative orientation of the interface with respect to the habit plane.

The parameters of the ferrite model have been identified by fitting the experimental stress-strain data in [48] and listed in Table 1. The parameters of the reduced lath martensite model used in [41] were based on a martensite carbon content ~ 0.4 wt.% C. In the tested grade, the martensite carbon content is estimated to be ~ 0.13 wt.% C. This entails a substantial decrease of the martensite hardness [49], whereas the austenite hardness is known to be much less sensitive to the carbon content [50]. Therefore, the material parameters of the martensite laths have been adjusted accordingly in Table 1. The parameters of the M/F interface damage indicator model are taken from [41].

The region of interest including the ferrite buffer layer, is discretized using 3D linear finite elements with one element in the out-of-plane direction and an average in-plane element size ~ 1 μm. The resulting discretization is shown in Fig. 2(d). Periodic boundary conditions are enforced in all three spatial directions. In-plane uniaxial tension along the positive X axis is applied. For the out-of-plane direction, different conditions including overall plane stress, overall plane strain and (point-wise) plane strain conditions, have been examined, revealing only minor influences on the simulation results. Only the results for the plane strain condition will therefore be presented.

The (accumulated) equivalent plastic strain maps of the region of interest predicted by the numerical simulation, are reported in Fig. 3(a). Highly heterogeneous plastic deformations are found in both ferrite and martensite phases, with comparable local strain levels. To rationalize these observations, the effective sliding of each martensite packet is computed in Fig. 3(b) (greyscale colorbar). The locations in the martensite islands that present a large apparent plasticity (Fig. 3(a)) correspond with the packets that have a large sliding factor (Fig. 1(f)) revealing a pronounced sliding activity (Fig. 3(b)). This shows that the substructure boundary sliding is indeed the favourable deformation mode for the martensite islands. To predict the M/F interface damage initiation, the effective interface damage indicators are evaluated and plotted at the corresponding interface locations in Fig. 3(b) (cyan-to-magenta colorbar). Multiple interface damage initiation sites can be observed near the martensite packets with a pronounced sliding activity. Note, however, that a pronounced sliding activity does not necessarily imply a high interface damage indicator level, since the latter depends strongly on the relative orientation of the interface with respect to the habit plane (see also [41]).

Next, the in-situ SEM micrographs, Fig. 3(c), are considered. Comparing Figs. 3(b) and (c) demonstrates an adequate qualitative agreement between the martensite island sliding activities predicted by the numerical simulation and those identified in the experiments. Extensive slip traces can be identified along the habit planes (Fig. 1(e)) of the martensite packets with a high sliding factor (Fig. 1(f)), experimentally demonstrating the sliding occurrence (see also [37]). Pronounced interface damage activities are visible in Fig. 3(c). Three mesoscopic M/F interfacial zones (boxes in Fig. 3(b)) with a high damage indicator level, are investigated in more detail. Tracking the corresponding regions in Fig. 3(c) together with the magnifications in Fig. 3(d), reveals that the laths slide along the substructure boundaries (black arrows) and gradually penetrate into the near-interface ferrite matrix, inducing strain localization (yellow arrows). This confirms that the interface damage initiation is indeed triggered by the substructure boundary sliding (see also [40]). As the loading proceeds, more sliding-triggered interface damage initiates, potentially leading to eventual interface separation (e.g. the green box). Furthermore, the red and green regions tend to initiate the interface damage earlier than the blue region. All these experimental observations are well predicted by the numerical simulation (Fig. 3(b)). Without incorporating the sliding mechanism, i.e. the RA films, the numerical simulation cannot reproduce the experimental observations of martensite plasticity and interface damage, see Supplementary material 1 for more details. Finally, notice that the interface damage can also develop due to severe localized ferrite plasticity alone, which, however, is only observed in very few regions (Fig. 3(c)).

The sliding activity in two martensite regions (orange triangles) is however underestimated by the numerical simulation, despite their high sliding favourability (Fig. 1(f)). As suggested in [37], this may

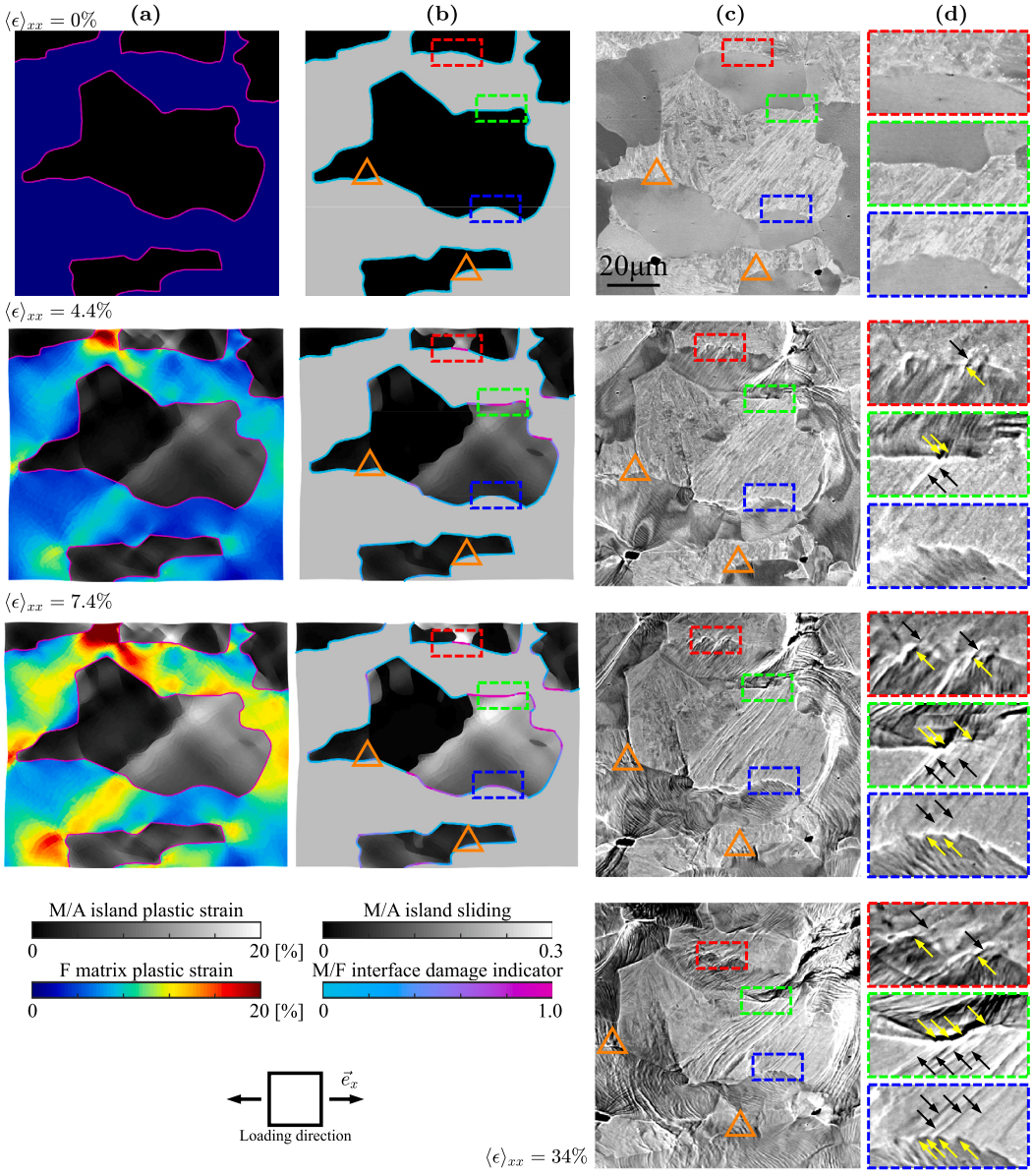

Fig. 3. Comparison between the numerical and experimental results for the DP steel region of interest at different levels of uniaxial tensile strain $\langle\epsilon\rangle_{xx}$: (a) the equivalent plastic strain maps; (b) the martensite island sliding maps (greyscale colorbar)) and the M/F interface damage indicators (cyan-to-magenta colorbar); (c) the in-situ SEM micrographs; (d) magnifications of three selected mesoscopic M/F interfacial zones (boxes), revealing the interface damage initiation (yellow arrows) triggered by the substructure boundary sliding (black arrows). Due to convergence limitations, the numerical simulation did not reach the final deformation stage ($\langle\epsilon\rangle_{xx} = 34\%$) as imposed in the experimental test. The two martensite regions with a sliding activity that is underestimated by the numerical simulation are indicated by the orange triangles in (b) and (c).

originate from the modelling assumption of an invariable (extruded) out-of-plane mesostructure in combination with the out-of-plane periodic boundary conditions. In reality, the subsurface mesostructure is unlikely to be constant through the out-of-plane direction. Moreover, Fig. 3(c) shows that the substructure boundary sliding occurrence is highly discrete and carried by a few substructure boundaries only [31,32,51]. This may be attributed to the presence of nano-precipitates or irregular lath morphology at some substructure boundaries [34], potentially obstructing the sliding activation. The substructure boundary sliding discreteness has not been included in the model. This could be incorporated in the future through a discrete slip plane model framework [52].

To enable a more quantitative comparison, the experimentally observed M/F interface damage initiation is further quantified based on the SEM micrographs. To this end, it is assumed that a higher image intensity contrast (i.e. greyscale value contrast) represents a higher strain localization [53] and thus a higher probability of damage initiation. At each sampled interface pixel, a circular interfacial zone with a radius R_{IZ} is defined and all greyscale values p belonging to the included ferrite region are collected into a set $\{p_F\}$. Two subsets, $\{p_F^H\}$ and $\{p_F^L\}$, representing the highest and lowest $\eta\%$ greyscale values over the whole $\{p_F\}$, are extracted. The contrast is then quantified using the absolute difference between the mean values of $\{p_F^H\}$ and $\{p_F^L\}$ as $C_{IZ} = |\bar{p}_F^H - \bar{p}_F^L|$. After standard min-max normalization to the range 0–1.0, C_{IZ} serves to quantify the M/F interface damage initiation in the experiments. The two parameters R_{IZ} and η are chosen as $R_{IZ} = 2$ μm and $\eta = 25$. It has been verified that different parameter choices lead to similar quantitative results for the interface damage initiation. More details can be found in Supplementary material 2.

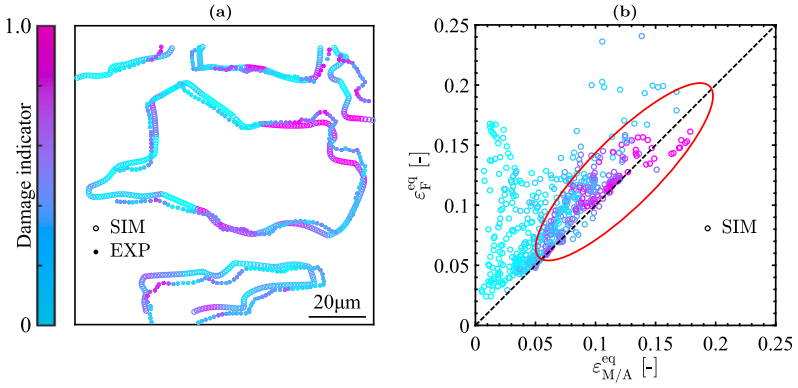

Fig. 4. (a) Comparison between the M/F interface damage indicator contours for the considered region of interest obtained by the numerical simulation (SIM) and the experimental analysis (EXP) at a uniaxial tensile strain of $\langle\epsilon\rangle_{xx} = 7.4\%$. The martensite islands and ferrite matrix are not displayed for clarity; (b) the predicted M/F interface damage indicator versus the near-interface ferrite and martensite equivalent strains. For reference, the black dashed line represents $\epsilon_{M/A}^{eq} = \epsilon_F^{eq}$. The region with a high damage indicator level is indicated by the red ellipse.

The M/F interface damage indicator contours predicted by the numerical simulation and quantified from the experiments are compared in Fig. 4(a). Despite a minor mismatch between the numerical and experimental deformed configurations, the damage indicator levels at most interface locations agree adequately. Since only the sliding-triggered interface damage initiation has been assumed in the model, this good agreement implies that the M/F interface damage initiation is indeed dominated by the substructure boundary sliding.

To gain additional insights on the correlation between the M/F interface damage initiation and the deformation of the bulk phases, the predicted interface damage indicators at all interface locations are plotted in Fig. 4(b) against the near-interface ferrite and martensite equivalent strains. Clearly, the M/F interface damage initiation seems to be accompanied by a low M/F strain partitioning, i.e. along the diagonal where the martensite and ferrite strains are comparable (red ellipse). This is in sharp contrast to most literature where the M/F interface damage occurrence has been presumed to be due to a high M/F strain partitioning considering the hard nature of martensite (e.g. [5–8]). Furthermore, it has been recently demonstrated that martensite can behave in a soft and ductile manner (see e.g. martensitic steels [31–33] and DP steels [34–37]). The intrinsic correlation found here between the M/F interface damage initiation and the low M/F strain partitioning (also supported by recent experimental observations [9–12]) emphasizes that the physical origin behind martensite ductility, i.e. substructure boundary sliding, induces a highly localized plasticity, and often damage, in the near-interface ferrite. This new understanding can be instrumental for fine tuning the microstructure to further optimize the well-known strength/ductility trade-off of DP steels.

To summarize, an integrated experimental-numerical study has been carried out to investigate M/F interface damage initiation, which is an importance failure mechanism in many DP steels that exhibit apparent martensite plasticity. The main findings include: (i) the substructure boundary sliding, which acts as the favourable deformation mode for the martensite islands, triggers and dominates M/F interface damage initiation accompanied by apparent martensite plasticity, as originally hypothesized in [39]; (ii) as a consequence, the M/F interface damage initiation correlates with a low M/F strain partitioning, rather than with pronounced M/F strain partitioning as commonly presumed in literature; (iii) the M/F interface damage indicator model developed in [41] based on the sliding-triggered interface damage initiation mechanism, enables efficient and quantitative predictions of the M/F interface damage initiation sites in DP steels.

Declaration of competing interest

The authors declare that they have no known competing financial interests or personal relationships that could have appeared to influence the work reported in this paper.

Acknowledgements

This research was carried out under project number T17019d in the framework of the research program of the Materials Innovation Institute (M2i) (www.m2i.nl) supported by the Dutch government. The authors gratefully acknowledge Roy L.A. Kerkhof for his experimental support and discussion.

Appendix A. Supplementary material

Supplementary material related to this article can be found online at https://doi.org/10.1016/j.scriptamat.2023.115798.

References

[1] C.C. Tasan, M. Diehl, D. Yan, M. Bechtold, F. Roters, L. Schemmann, C. Zheng, N. Peranio, D. Ponge, M. Koyama, K. Tsuzaki, D. Raabe, An overview of dual-phase steels: advances in microstructure-oriented processing and micromechanically guided design, Annu. Rev. Mater. Res. 45 (2015) 391–431.
[2] G. Avramovic-Cingara, Ch.A.R. Saleh, M.K. Jain, D.S. Wilkinson, Void nucleation and growth in dual-phase steel 600 during uniaxial tensile testing, Metall. Mater. Trans. A 40 (2009) 3117–3127.
[3] C. Landron, E. Maire, O. Bouaziz, J. Adrien, L. Lecarme, A. Bareggi, Validation of void growth models using x-ray microtomography characterization of damage in dual phase steels, Acta Mater. 59 (2011) 7564–7573.
[4] K. Isik, G. Gerstein, T. Clausmeyer, F. Nürnberger, A.E. Tekkaya, H.J. Maier, Evaluation of void nucleation and development during plastic deformation of dual-phase steel dp600, Steel Res. Int. 87 (2016) 1583–1591.
[5] D. Das, P.P. Chattopadhyay, Influence of martensite morphology on the work-hardening behavior of high strength ferrite–martensite dual-phase steel, J. Mater. Sci. 44 (2009) 2957–2965.
[6] J. Kadkhodapour, A. Butz, S. Ziaei Rad, Mechanisms of void formation during tensile testing in a commercial, dual-phase steel, Acta Mater. 59 (2011) 2575–2588.
[7] T. Matsuno, C. Teodosiu, D. Maeda, A. Uenishi, Mesoscale simulation of the early evolution of ductile fracture in dual-phase steels, Int. J. Plast. 74 (2015) 17–34.
[8] A. Tang, H. Liu, R. Chen, G. Liu, Q. Lai, Y. Zhong, L. Wang, J. Wang, Q. Lu, Y. Shen, Mesoscopic origin of damage nucleation in dual-phase steels, Int. J. Plast. 137 (2021) 102920.
[9] H. Ghadbeigi, C. Pinna, S. Celotto, Failure mechanisms in dp600 steel: initiation, evolution and fracture, Mater. Sci. Eng. A 588 (2013) 420–431.
[10] M. Calcagnotto, Y. Adachi, D. Ponge, D. Raabe, Deformation and fracture mechanisms in fine- and ultrafine-grained ferrite/martensite dual-phase steels and the effect of aging, Acta Mater. 59 (2011) 658–670.
[11] Q. Lai, O. Bouaziz, M. Gouné, A. Perlade, Y. Bréchet, T. Pardoen, Microstructure refinement of dual-phase steels with 3.5wt% Mn: influence on plastic and fracture behavior, Mater. Sci. Eng. A 638 (2015) 78–89.

[12] H. Ghadbeigi, C. Pinna, S. Celotto, J.R. Yates, Local plastic strain evolution in a high strength dual-phase steel, Mater. Sci. Eng. A 527 (2010) 5026–5032.
[13] G. Krauss, Martensite in steel: strength and structure, Mater. Sci. Eng. A 273–275 (1999) 40–57.
[14] S. Morito, H. Tanaka, R. Konishi, T. Furuhara, T. Maki, The morphology and crystallography of lath martensite in Fe-C alloys, Acta Mater. 51 (2003) 1789–1799.
[15] S. Morito, X. Huang, T. Furuhara, T. Maki, N. Hansen, The morphology and crystallography of lath martensite in alloy steels, Acta Mater. 54 (2006) 5323–5331.
[16] M. Erdogan, The effect of new ferrite content on the tensile fracture behaviour of dual phase steels, J. Mater. Sci. 37 (2002) 3623–3630.
[17] Q. Lai, O. Bouaziz, M. Gouné, L. Brassart, M. Verdier, G. Parry, A. Perlade, Y. Bréchet, T. Pardoen, Damage and fracture of dual-phase steels: influence of martensite volume fraction, Mater. Sci. Eng. A 646 (2015) 322–331.
[18] J.P.M. Hoefnagels, C.C. Tasan, F. Maresca, F.J. Peters, V.G. Kouznetsova, Retardation of plastic instability via damage-enabled microstrain delocalization, J. Mater. Sci. 50 (2015) 6882–6897.
[19] F. Archie, X. Li, S. Zaefferer, Micro-damage initiation in ferrite-martensite dp microstructures: a statistical characterization of crystallographic and chemical parameters, Mater. Sci. Eng. A 701 (2017) 302–313.
[20] B. Chehab, X. Wang, J-P. Masse, O. Bouaziz, H. Zurob, D. Embury, Bulk nanoscale materials in steel products, J. Phys. Conf. Ser. 240 (2010) 012135.
[21] C. Du, J.P.M. Hoefnagels, S. Kölling, M.G.D. Geers, J. Sietsma, R. Petrov, V. Bliznuk, P.M. Koenraad, D. Schryvers, B. Amin-Ahmadi, Martensite crystallography and chemistry in dual phase and fully martensitic steels, Mater. Charact. 139 (2018) 411–420.
[22] B.P.J. Sandvik, C.M. Wayman, Crystallography and substructure of lath martensite formed in carbon steels, Metallography 16 (1983) 199–227.
[23] P.M. Kelly, A. Jostsons, R.G. Blake, The orientation relationship between lath martensite and austenite in low carbon, low alloy steels, Acta Metall. Mater. 38 (1990) 1075–1081.
[24] S. Morito, K. Oh-ishi, K. Hono, T. Ohba, Carbon enrichment in retained austenite films in low carbon lath martensite steel, ISIJ Int. 51 (2011) 1200–1202.
[25] X. Liao, X. Wang, Z. Guo, M. Wang, Y. Wu, Y. Rong, Microstructures in a resistance spot welded high strength dual phase steel, Mater. Charact. 61 (2010) 341–346.
[26] H. Yoshida, S. Takagi, S. Sakai, S. Morito, T. Ohba, Crystallographic analysis of lath martensite in ferrite-martensite dual phase steel sheet annealed after cold-rolling, ISIJ Int. 55 (2015) 2198–2205.
[27] F. Maresca, V.G. Kouznetsova, M.G.D. Geers, On the role of interlath retained austenite in the deformation of lath martensite, Model. Simul. Mater. Sci. Eng. 22 (2014) 045011.
[28] F. Maresca, V.G. Kouznetsova, M.G.D. Geers, Subgrain lath martensite mechanics: a numerical–experimental analysis, J. Mech. Phys. Solids 73 (2014) 69–83.
[29] F. Maresca, W.A. Curtin, The austenite/lath martensite interface in steels: structure, athermal motion, and in-situ transformation strain revealed by simulation and theory, Acta Mater. 134 (2017) 302–323.
[30] F. Maresca, V.G. Kouznetsova, M.G.D. Geers, W.A. Curtin, Contribution of austenite-martensite transformation to deformability of advanced high strength steels: from atomistic mechanisms to microstructural response, Acta Mater. 156 (2018) 463–478.
[31] C. Du, J.P.M. Hoefnagels, R. Vaes, M.G.D. Geers, Plasticity of lath martensite by sliding of substructure boundaries, Scr. Mater. 120 (2016) 37–40.
[32] J. Inoue, A. Sadeghi, T. Koseki, Slip band formation at free surface of lath martensite in low carbon steel, Acta Mater. 165 (2019) 129–141.
[33] H. Ghaffarian, Y. Na, D. Jang, Interfacial plasticity mediated by lath boundaries in reduced-activation ferritic/martensitic steels, J. Nucl. Mater. 559 (2022) 153439.
[34] C. Du, R. Petrov, M.G.D. Geers, J.P.M. Hoefnagels, Lath martensite plasticity enabled by apparent sliding of substructure boundaries, Mater. Des. 172 (2019) 107646.
[35] C. Tian, D. Ponge, L. Christiansen, C. Kirchlechner, On the mechanical heterogeneity in dual phase steel grades: activation of slip systems and deformation of martensite in dp800, Acta Mater. 183 (2020) 274–284.
[36] F. Briffod, H. Hu, T. Shiraiwa, M. Enoki, Effect of in-lath slip strength on the strain partitioning in a dual-phase steel investigated by high-resolution digital image correlation and crystal plasticity simulations, Mater. Sci. Eng. A 862 (2023) 144413.
[37] V. Rezazadeh, R.H.J. Peerlings, T. Vermeij, J.P.M. Hoefnagels, F. Maresca, M.G.D. Geers, Extensive anisotropic lath martensite plasticity in dual-phase steels: a numerical-experimental investigation, 2023, in preparation; available on arXiv: https://doi.org/10.48550/arXiv.2211.08331.
[38] T. Vermeij, C.J.A. Mornout, V. Rezazadeh, J.P.M. Hoefnagels, Martensite plasticity and damage competition in dual-phase steel: a micromechanical experimental–numerical study, Acta Mater. 254 (2023) 119020.
[39] L. Liu, F. Maresca, J.P.M. Hoefnagels, T. Vermeij, M.G.D. Geers, V.G. Kouznetsova, Revisiting the martensite/ferrite interface damage initiation mechanism: the key role of substructure boundary sliding, Acta Mater. 205 (2021) 116533.
[40] T. Vermeij, R.L.A. Kerkhof, J.P.M. Hoefnagels, Favorable lath martensite plasticity mechanisms in dual-phase steel: substructure boundary sliding and habit plane slip, 2023, in preparation.
[41] L. Liu, F. Maresca, J.P.M. Hoefnagels, M.G.D. Geers, V.G. Kouznetsova, A multi-scale framework to predict damage initiation at martensite/ferrite interface, J. Mech. Phys. Solids 168 (2022) 105018.
[42] R. Roumina, M. Bruhis, J.P. Masse, H.S. Zurob, M. Jain, O. Bouaziz, J.D. Embury, Bending properties of functionally graded 300M steels, Mater. Sci. Eng. A 653 (2016) 63–70.
[43] W.C. Lenthe, S. Singh, M. De Graef, A spherical harmonic transform approach to the indexing of electron back-scattered diffraction patterns, Ultramicroscopy 207 (2019) 112841.
[44] F. Niessen, T. Nyyssönen, A.A. Gazder, R. Hielscher, Parent grain reconstruction from partially or fully transformed microstructures in mtex, J. Appl. Crystallogr. 55 (2022) 180–194.
[45] R. Hielscher, T. Nyyssönen, F. Niessen, A.A. Gazder, The variant graph approach to improved parent grain reconstruction, Materialia 22 (2022) 101399.
[46] M. Diehl, P. Shanthraj, P. Eisenlohr, F. Roters, Neighborhood influences on stress and strain partitioning in dual-phase microstructures, Meccanica 51 (2016) 429–441.
[47] F. Maresca, V.G. Kouznetsova, M.G.D. Geers, Reduced crystal plasticity for materials with constrained slip activity, Mech. Mater. 92 (2016) 198–210.
[48] F. Lani, Q. Furnémont, T. Van Rompaey, F. Delannay, P.J. Jacques, T. Pardoen, Multiscale mechanics of trip-assisted multiphase steels: II. micromechanical modelling, Acta Mater. 55 (2007) 3695–3705.
[49] T. Niino, J. Inoue, M. Ojima, S. Nambu, T. Koseki, Effects of solute carbon on the work hardening behavior of lath martensite in low-carbon steel, ISIJ Int. 57 (2017) 181–188.
[50] H.K.D.H. Bhadeshia, R. Honeycombe, Steels: Microstructure and Properties, Elsevier, 2006.
[51] T. Vermeij, J.A.C. Verstijnen, T.J.J. Ramirez y Cantador, B. Blaysat, J. Neggers, J.P.M. Hoefnagels, A nanomechanical testing framework yielding front&rear-sided, high-resolution, microstructure-correlated sem-dic strain fields, Exp. Mech. 62 (2022) 1625–1646.
[52] J. Wijnen, R.H.J. Peerlings, J.P.M. Hoefnagels, M.G.D. Geers, A discrete slip plane model for simulating heterogeneous plastic deformation in single crystals, Int. J. Solids Struct. 228 (2021) 111094.
[53] A. Weidner, H. Biermann, Review on strain localization phenomena studied by high-resolution digital image correlation, Adv. Eng. Mater. 23 (2021) 2001409.